

Article

Alloy Optimization for Reducing Delayed Fracture Sensitivity of 2000 MPa Press Hardening Steel

Hardy Mohrbacher ^{1,2,*}  and Takehide Senuma ³¹ NiobelCon BV, B-2970 Schilde, Belgium² Department of Materials Engineering (MTM), KU Leuven, B-3001 Heverlee, Belgium³ Department of Mechanical and Systems Engineering, Okayama University, Okayama 700-8530, Japan; senuma@mech.okayama-u.ac.jp

* Correspondence: hm@niobelcon.net; Tel.: +32-3484-5260

Received: 8 June 2020; Accepted: 26 June 2020; Published: 28 June 2020



Abstract: Press hardening steel (PHS) is widely applied in current automotive body design. The trend of using PHS grades with strengths above 1500 MPa raises concerns about sensitivity to hydrogen embrittlement. This study investigates the hydrogen delayed fracture sensitivity of steel alloy 32MnB5 with a 2000 MPa tensile strength and that of several alloy variants involving molybdenum and niobium. It is shown that the delayed cracking resistance can be largely enhanced by using a combination of these alloying elements. The observed improvement appears to mainly originate from the obstruction of hydrogen-induced damage incubation mechanisms by the solutes as well as the precipitates of these alloying elements.

Keywords: hydrogen damage mechanisms; austenite grain size; precipitation; grain boundary cohesion; vacancy complexes; solute segregation

1. Introduction

In current car body design processes, press hardening steel (PHS) plays a prominent role with regard to crash intrusion resistance and weight reduction. As a standard, steel grade 22MnB5 containing around 0.22% carbon is used for producing components of 1500 MPa tensile strength. The alloying elements, i.e., manganese, boron and titanium, that are added to this steel provide sufficient hardenability in the press hardening process, which is also known under the term “hot stamping”. In this process, the steel sheet is heated up into the austenitic phase immediately before stamping. Forming occurs in the austenitic state at over 800 °C. The forming die acts as a heat sink, quenching the hot steel upon reaching full contact pressure. A sufficiently high quenching rate, usually >30 °C/s, in combination with Mn-B-Ti alloying, results in the transformation from austenite into martensite. During paint baking at the end of the body production cycle, typically performed at around 170 °C for the duration of 20 min, the as-quenched martensitic press-hardened steel experiences low-temperature tempering. Thereby, the tensile strength moderately decreases while the yield strength increases.

With the share of 1500 MPa PHS reaching 30%–40% of the total body weight in some car models, the possible weight reduction potential is approaching a limit. However, further weight reduction becomes feasible when using PHS grades stronger than 1500 MPa. In this respect, grade 30MnB5, containing 0.30% carbon, was developed for producing components with 1800 MPa tensile strength. To meet minimum impact toughness requirements at low service temperatures, niobium microalloying was introduced [1,2]. Niobium-based precipitates limit the austenite grain size before quenching, resulting in improved toughness performance [3]. More recent PHS development activities aim to achieve a tensile strength of 2000 MPa. The base alloy concept for these steel grades is 34MnB5, i.e., the carbon content is further increased to around 0.34%. The first commercially available grades

of 2000 MPa PHS employed niobium microalloying in combination with molybdenum alloying [4]. Molybdenum additionally contributes to prior austenite grain refinement and appears to be particularly beneficial for reducing hydrogen embrittlement in these steels [5].

Ultra-high strength steels such as PHS grades are sensitive to failure caused by the hydrogen which accumulates in the microstructure [6,7]. The failure scenarios involve more specific processes such as stress corrosion cracking (SCC), corrosion fatigue cracking (CFC) and hydrogen-induced cracking (HIC), also referred to as hydrogen embrittlement (HE). The embrittlement manifests itself as non-ductile fracture features, poor elongation and reduced tensile strength.

In hydrogen embrittled martensitic steel, isolated areas can be observed by exposing either intergranular (Figure 1a) or transgranular (Figure 1b) fractures, depending on the relative strength of the grain boundaries and interfaces [8]. The higher the strength of the steel, the greater its susceptibility to HE and the lower the tolerable amount of diffusible hydrogen content. At these higher strength levels, the local hydrogen distribution appears to be a more relevant criterion than the bulk average diffusible hydrogen content. Consequently, countermeasures to HE should not only focus on reinforcing boundary strength but also on preventing the local aggregation of hydrogen. Important mechanisms in this respect are microstructural refinement and hydrogen trapping by precipitates, as well as reducing the mobility of dislocations or vacancies. From an alloy design point of view, niobium and molybdenum are elements that can contribute to enabling all of these preventive mechanisms [9]. Other alloying elements (e.g., Mn), as well as impurities (e.g., P, S and N), can cause negative effects such as decreased cohesion of grain boundaries and interfaces or the formation of larger-sized particles; for instance, MnS and TiN [10,11]. Respective metallurgical solutions have been implemented in various applications that were using ultra-high strength martensitic steels long before they were considered for car body components. Abrasion-resistant plates, bolts, casings, chains or springs can be named as examples. Often, Mo alloying, as well as Nb microalloying, in such applications was shown to significantly extend the time-to-fracture under hydrogen charging conditions [9].

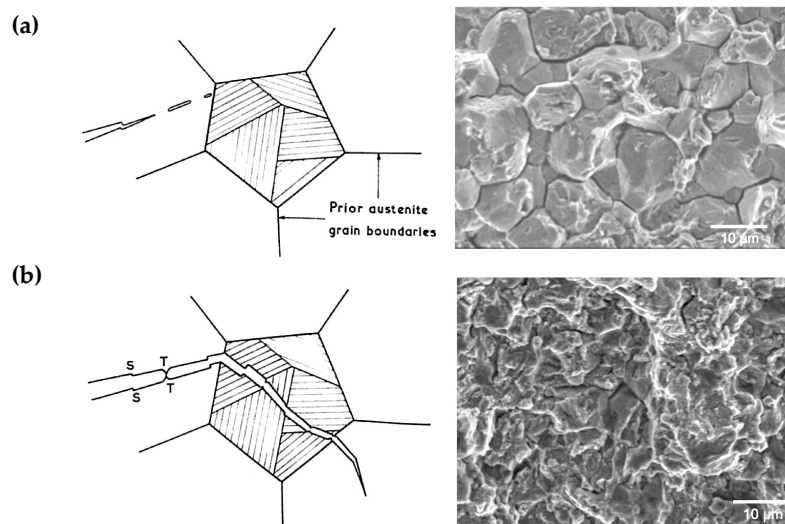


Figure 1. Appearance of brittle fracture after mild hydrogen charging of martensitic steel. (a) Intergranular fracture path is along prior austenite grain boundaries and martensite packet boundaries caused by hydrogen-enhanced grain boundary decohesion (HEDE); (b) Transgranular fracture path along lath boundaries accompanied by trans-lath steps (S), localized plastic tearing (T) by dislocation pile-up and hydrogen-enhanced local plasticity (HELP).

The damage phenomenon of delayed fracture is related to hydrogen embrittlement. The applied or residual stress that acts in a component, in combination with the hydrogen dissolved in the steel, can lead to cracking after a time delay. During this delay time, hydrogen diffuses within the steel matrix and locally aggregates in microstructural features, incubating and initiating damage that finally propagates

into macroscopic failure. Thus, the HE resistance of a steel can be characterized by the time-to-fracture measured under defined static stress and hydrogen charging conditions. Such test conditions are used in the present investigation for benchmarking and optimizing alloy concepts that are being developed for 2000 MPa PHS grades. Beyond simply aiming at increased time-to-fracture performance values, it is important to understand the interaction of alloying elements with hydrogen and the potential damage mechanisms. Alloying elements can interfere with hydrogen either directly, by lowering its mobility in the iron lattice, or indirectly, by obstructing damage mechanisms. Hydrogen-enhanced grain boundary decohesion (HEDE), hydrogen-enhanced local plasticity (HELP) and hydrogen-enhanced strain-induced vacancy mechanisms (HESIV) have been proposed as the key mechanisms involved in causing delayed fractures in martensitic steel.

The HEDE mechanism hypothesizes that hydrogen weakens the cohesion of a grain boundary after segregating to it [11–13]. An initiated crack propagates along the grain boundary if its cohesion is substantially compromised, leading to grain boundary (intergranular) fracture (Figure 1a). This fracture appearance can indeed be observed, particularly after the severe hydrogen charging of martensite with a coarse prior austenite grain structure [14]. Impurities as well as certain alloying elements, e.g., phosphorous and manganese [15–17], additionally reduce coherency when segregated to the prior austenite grain boundary, thereby enhancing the deleterious effect of hydrogen. On the other hand, some typical alloying elements that are used in ultra-high strength steels such as Nb, Mo, Ti and W have the effect of increasing boundary cohesion when segregated to it [16,17]. In the wider sense, the principles of the HEDE hypothesis similarly hold for interfaces between inclusions and the steel matrix. When such interfaces act as damage initiation sites, fractures can have a ductile appearance, since inclusions typically act as nucleation sites for the characteristic dimples.

Intragranular failure often appears as a quasi-cleavage fracture. Under the conditions of low-temperature embrittlement, the fracture path is found along lath boundaries involving trans-lath steps, consistent with the {100} cleavage planes, as shown in Figure 1b. Nagao et al. [18], however, pointed out that the fracture path of a hydrogen-induced “quasi-cleavage” fracture typically involves {110} slip planes, while beneath the fracture surface, extensive plasticity in the form of intense slip bands and the partial destruction of lath boundaries is observed. An explanation for the intense plasticity can be found in the HELP hypothesis [19], which postulates that the mobility of dislocations increases due to the interaction of the elastic stress field generated by hydrogen with that caused by the dislocations. As a result of the stress release, the propagation rate of a microcrack, which depends on the mobility of dislocations nucleating in the fracture process zone at its tip, is accelerated. On the other hand, the distance between dislocations piled up against the grain boundary is reduced and the stress acting on the boundary is increased, accelerating crack initiation at the grain boundary.

In the HESIV hypothesis, hydrogen is considered to only indirectly cause delayed cracking [20]. The proposed mechanism ascribes to hydrogen the primary role of suppressing the annihilation of supersaturated vacancies originating from dislocation, climbing and cutting with each other during deformation [21]. These stabilized supersaturated vacancies promote void nucleation and reduce the resistance to crack growth. Hydrogen also lowers the activation energy for the formation of vacancies, leading to the higher density of the supersaturated vacancies. This hypothesis is very promising for explaining the hydrogen embrittlement observed at slow strain rate tensile testing, because heavy plastic deformation occurs, and a high amount of supersaturated vacancies is being created and stabilized.

It is likely that several of the mentioned mechanisms act individually or in combination when a steel sample is subjected to delayed cracking test conditions. This is due to microstructural and chemical inhomogeneities and the actual grain orientation with respect to the acting applied stress, as well as locally varying residual stress states which are present in the steel.

The current work aims at improving a 0.33% C-Mn-B-Ti base alloy concept that is typically used for 2000 MPa PHS in order to achieve superior resistance against hydrogen-induced delayed cracking. In this approach, molybdenum is added in amounts of up to 0.5% and additionally combined with 0.05%

Nb microalloying. The observations regarding delayed fracture resistance will be discussed in the light of microstructural details and the possible interaction of alloying elements with hydrogen-induced damage mechanisms. This should allow us to make recommendations for the alloy and processing design of 2000 MPa PHS grades.

2. Materials and Methods

2.1. Experimental Steel Production and Treatment

All alloy variants investigated in this study use the same base alloy platform of 0.33 mass percent carbon in combination with Mn-B-Ti alloying, as is typically used for press hardening steels (Table 1). The chosen carbon content is a pre-requisite for achieving a tensile strength level of 2000 MPa [3]. Alloy variants investigate the effect of increasing molybdenum levels, as well as niobium microalloying, in combination with molybdenum.

Table 1. Chemical composition (mass percent) of experimental 2000 MPa press hardening steels.

Steel	C	Si	Mn	P	S	Al	N	B	Ti	Mo	Nb
Base	0.33	0.1	1.2	0.005	0.005	0.04	0.002	0.002	0.02	-	-
+Mo	0.33	0.1	1.2	0.005	0.005	0.04	0.002	0.002	0.02	0.15–0.5	-
+Nb	0.33	0.1	1.2	0.005	0.005	0.04	0.002	0.002	0.02	0.15	0.05
	0.32	0.1	1.2	0.001	0.002	0.04	0.0007	0.002	0.02	0.5	0.05

The experimental steel alloys were liquefied in a vacuum furnace and cast into ingots of 50 kg in weight. Subsequently, the ingots were reheated at 1250 °C for 60 min and subjected to a treatment cycle that simulated industrial processing conditions (Figure 2). After hot rolling the ingots to a 3 mm gage using a finishing temperature of around 930 °C, the hot strips were immediately transferred into an electrical furnace and kept for 60 min at either 600 °C or 400 °C. The isothermal holding was followed by slow cooling to room temperature after switching off the furnace. This procedure simulated either a higher (600 °C) or lower (400 °C) coiling temperature. Accordingly, the hot strips revealed a ferritic-pearlitic or bainitic microstructure, respectively. After pickling, the hot strips were cold rolled to 1.4 mm thick sheets. The cold rolled steel sheets were subsequently heat treated using a direct current heating device, thereby simulating two possible hot stamping process variants. In a flash heat treatment cycle (designated as “short”), the samples were heated with a rate of 10 °C/s to a peak temperature of 875 °C and then immediately water quenched. The conventional hot stamping cycle (designated as “long”) was simulated by soaking the steel at 900 °C for 300 s, followed by water quenching. Combinations of these processing conditions were intended to vary grain sizes and to influence the precipitation as well as the alloy segregation status. All quenched samples were subsequently aged at 170 °C for 20 min, simulating the paint baking cycle (bake hardening treatment) that is typically applied in automotive body production. Some cold rolled samples of the base alloy were also austenitized at higher temperatures (1000–1200 °C) in order to provoke coarser austenite grain sizes.

It is important to note here that the conditioning of the material and the related test results originating from this study represent the steel performance during the vehicle use phase. Many published results on the hydrogen embrittlement of PHS, on the contrary, refer to the as-quenched state, i.e., before the bake hardening treatment. Such results obtained in the as-quenched condition represent the intermediate phase, between the press shop and final assembly.

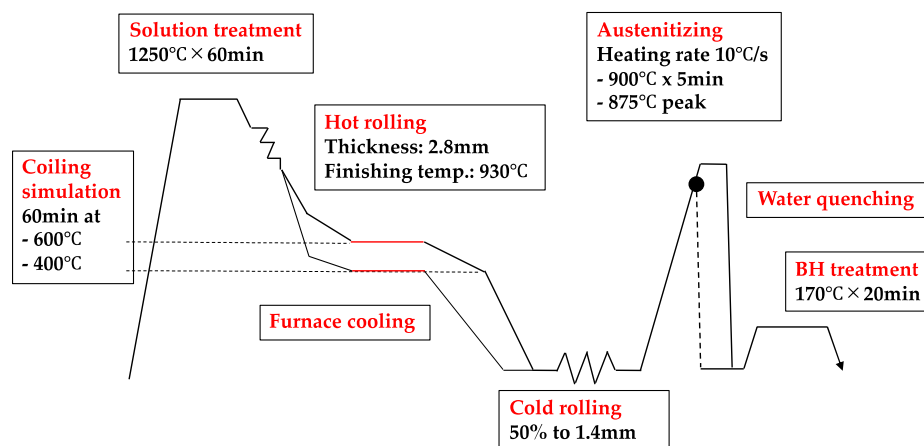


Figure 2. Thermo-mechanical treatment schedule for sample production of press hardening steel.

2.2. Mechanical Characterization

Before mechanical testing, the originally 1.4 mm thick heat-treated steel samples were machined down to 1.0 mm gages to exclude disturbing influences caused by the potential decarburization of the surface-near layer during heat treatment. Tensile testing was performed using the samples, according to Japanese standard JIS 13B in a standard tensile test machine type AG-50kNXplus (Shimadzu Ltd., Kyoto, Japan).

The equipment and the sample geometry used to perform the delayed cracking tests is shown in Figure 3. During these tests, the samples were immersed in a 10% ammonium thiocyanate solution while applying a maximum notch stress of 1300 MPa. The time-to-fracture was measured. Since the data scattering of such measurements was relatively large, the delayed cracking tests were repeated up to seven times for each alloy and processing condition in order to obtain reliable average values.

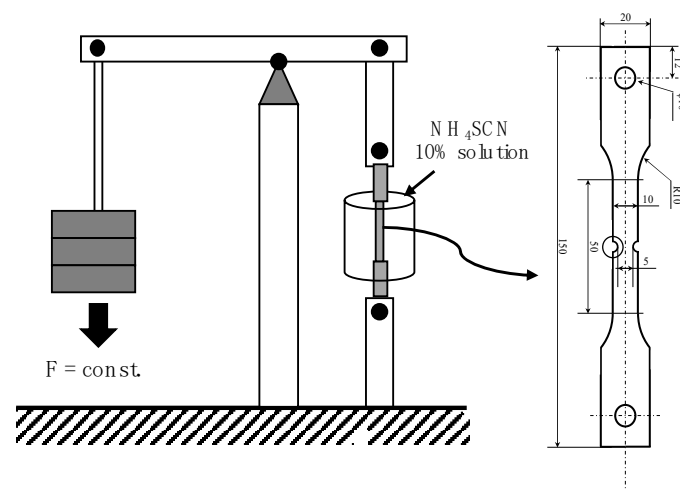


Figure 3. Experimental setup and geometry of notched tensile sample used for delayed cracking testing under constant load conditions.

2.3. Microstructural Characterization

Observations of microstructure were conducted using optical microscopy (OM) and scanning electron microscopy (SEM), JSM-700IF (JEOL, Peabody, MA, USA). Transmission electron microscopy (TEM) was used to determine the size and distribution of the precipitates. TEM foils were prepared by the standard twin-jet electropolishing method with an applied voltage of 20 V, using a 300 mL methanol, 180 mL n-butanol, and 30 mL perchloric acid electrolyte at -40°C . TEM observation and

bright-field (BF), dark-field (DF) and selected area diffraction (SAD) imaging were performed using Topcon EM-002B (Topcon Corporation, Tokyo, Japan) operated at 160 kV.

The microtexture data obtained by electron back-scattering diffraction (EBSD) (Topcon Corporation, Tokyo, Japan) analysis were used to determine the grain size of the martensite. The martensitic grain size was evaluated from the measured data using an evaluation procedure developed by Miyamoto et al. [22].

Atom probe tomography was performed to identify the degree of grain boundary segregation in the alloying elements. The measurements utilized the laser mode of a local electrode atom probe with high-angle reflection (LEAP X4000X HR, Cameca Instruments, Gennevilliers, France), at a frequency of 250 kHz and a pulse energy of 30 pJ. The specimen was kept at a temperature of 50 K.

2.4. Measurement of Hydrogen Accumulation

The saturation potential of hydrogen accumulation in the bulk material was measured by immersing samples in a 10% ammonium thiocyanate solution for 48 h. The total amount of hydrogen accumulated in the steel was then determined by thermal desorption analysis (TDA), with an applied heating rate of 200 °C/h, using a gas chromatograph JTF-20AH (J-Science, Tokyo, Japan). The TDA measurements were repeated between two and five times for each of the alloy variants.

3. Results

3.1. Alloy Effects on Strength and Hardenability

The tensile strength for the heat treated (short cycle) and bake hardened steels is shown in Figure 4. The as-quenched strength of the base alloy was calculated from the carbon content of 2040 and 2075 MPa for 0.32 and 0.33% C, respectively, as described in [3]. The baking treatment, acting as a low-temperature tempering measure, reduced the tensile strength by around 130 MPa. Molybdenum alloying contributed to the tensile strength by solid solution strengthening and grain refinement, as well as by providing tempering resistance. For the higher coiling temperature (600 °C), the strength increased almost linearly with the molybdenum content. For the lower coiling temperature (400 °C), tensile strength remained on an equally high level, irrespective of the molybdenum content. This could have been due to the prior austenite grain size as well as to solid solution strengthening by molybdenum. The lower coiling temperature apparently led to a higher solid solution strengthening effect for the lower molybdenum content levels.

The combined addition of 0.05% Nb and 0.15% Mo raised the strength by about 50 MPa. Niobium microalloying provided additional grain refinement by the precipitation of NbC particles, restricting austenite grain growth via boundary pinning. On the other hand, Nb precipitation consumed a small amount of carbon. Assuming the exact stoichiometric ratio between Nb and C to be 7.74:1, approximately 65 ppm carbon was removed from the matrix, corresponding to a strength loss of around 25 MPa. The 0.5% Mo-0.05% Nb alloy as such had a lower base carbon content (0.32% C), accounting for approximately 35 MPa strength loss. Thus, the total strength loss related to carbon was around 60 MPa.

Generally, all present alloy combinations securely achieved the required minimum tensile strength for a 2000 MPa PHS grade. It should be emphasized that water quenching was applied in the present laboratory trials. The die quenching used in the industrial hot stamping process provides a less severe cooling rate, likely resulting in slightly lower tensile strength values when using standard Mn-B-Ti grades. Molybdenum alloying in combination with boron significantly reduces the critical cooling rate for full martensite transformation [23], thus enhancing the process' robustness under industrial conditions.

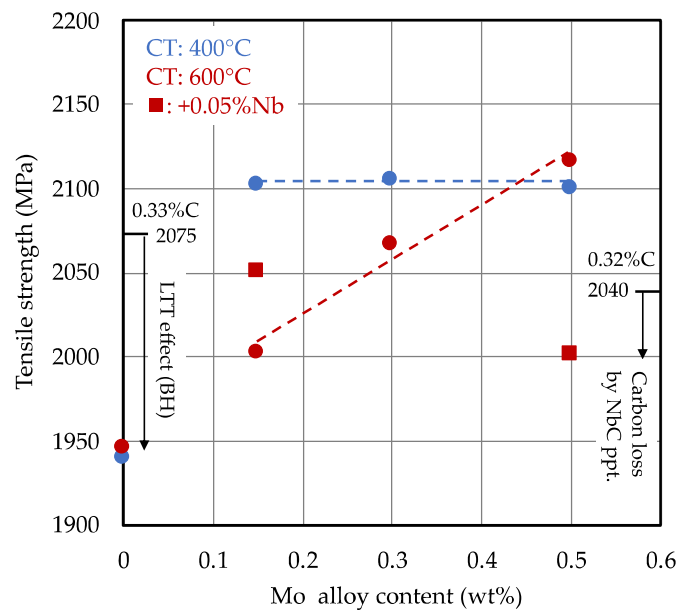


Figure 4. Effect of molybdenum and niobium alloy content on tensile strength after water quenching and bake hardening treatment (CT: coiling temperature; short heating cycle); as-quenched base strength is calculated according to [3], with permission from authors, 2018.

Hardenability is a property that is of the highest importance to PHS, essential for achieving the desired fully martensitic microstructure under industrial hot-stamping conditions. Standard PHS grades rely on boron microalloying to reduce the critical cooling rate to values of around 30 °C/s. Molybdenum alloying is known to provide excellent hardenability by itself and to synergistically enhance the effect of boron. According to a recent study by Ishikawa et al. [24], molybdenum additions below 0.75% suppress the precipitation of $\text{Fe}_{23}(\text{C}, \text{B})_6$ during cooling, thus enhancing the potency of boron for blocking ferrite nucleation. The transformation behavior from full austenite under a cooling rate of 10 °C/s was derived from dilatometer tests and is shown in Figure 5a for the base alloy and the Mo-alloyed variants. It is apparent that the addition of molybdenum to the base alloy significantly retarded the transformation in the bainitic temperature range, particularly when the molybdenum content exceeded 0.3%. The change in the martensite's start temperature by molybdenum additions in the current range was, however, very small (<5 °C). With regard to practical applications, the delay of bainite formation by sufficient molybdenum addition extends the possible processing window for hot-stamping operations. A wider applicable temperature range for executing hot-forming facilitates the potential use of zinc coatings. The melting temperature of zinc is below the typical austenitizing temperature. The delay of transformation by Mo alloying enables process modifications, allowing zinc to solidify before stamping. Moreover, the applicable time window for multi-step hot-forming operations using a transfer press system becomes wider due to the Mo-induced transformation delay.

The coiling temperature had a remarkable influence on the transformation behavior of the Mo alloyed steels (Figure 5b). The transformation became increasingly retarded for the lower coiling temperature steel as it proceeded from the initial austenite grain boundary site towards the interior of the grain. The 0.3% Mo addition even revealed a pronounced stasis at a transformation level of around 80%. After the stasis, the transformation continued below the martensite start temperature for the remaining austenite fraction. The slower transformation kinetics for steels produced at lower coiling temperatures suggests that solute molybdenum was distributed more homogeneously within the prior austenite grain. The progressing transformation front was progressively enriching, with solute molybdenum atoms exerting increasing solute drag on the phase front. In the steels produced at higher coiling temperatures, molybdenum was expected to be more noticeably segregated to the austenite grain boundary area. Thus, the observed transformation kinetics allows conclusions on

the distribution of solute molybdenum within the austenite grain, which is important with respect to the later discussion.

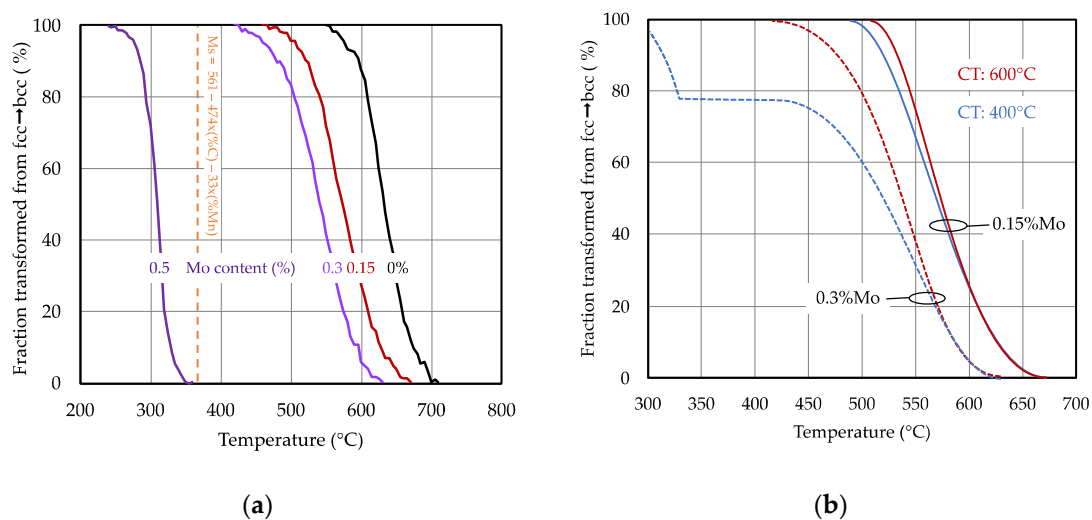


Figure 5. (a) Effect of molybdenum alloy content on the fcc-bcc transformation behavior (coiling temperature: 600 °C, heating rate: 10 °C/s, peak temperature: 875 °C, cooling rate: 10 °C/s); (b) influence of coiling temperature (CT) on the transformation behavior of 0.15 and 0.3% Mo alloyed steel (curves smoothed for clarity).

3.2. Alloy Effects on Microstructure

The microstructure of the quenched steels was characterized using EBSD based techniques. Figure 6a shows inverse pole figures (IPF) for the two heat treatment procedures and the alloy range. For the short heat treatment cycle, no significant difference in the microstructure was seen over the alloy range. On the contrary, the standard heat treatment revealed a coarser substructure, with pronounced lath-like features in the Mo-free steel, while the Mo-alloyed steels had a substructure similar to those seen with the short heat treatment. The prior austenite grains were reconstructed from the EBSD analysis. The prior austenite grain size (PAGS) shown in Figure 6b was largest in the base alloy, reaching average values of 14–18 μm for the standard heat treatment and only 6 μm for the short heat treatment. Molybdenum alloying reduced the PAGS to average values of around 6 μm for the standard soaking treatment and 4 μm for the flash treatment for all Mo contents. Smaller PAGS values for the short heat treatment are reasonable, since the short residence time in the austenite phase field did not allow substantial growth of the austenite grains. Under standard heat treatment conditions, the PAGS was further refined by additional niobium microalloying, i.e., from 8.4 μm to 4.6 μm in the 0.15% Mo steel and from 5.4 μm to 4.6 μm in the 0.5% Mo steel. The efficient control of PAGS by niobium microalloying during such heat treatments is related to the existence of stable NbC precipitates that exert strong boundary pinning [3]. Molybdenum, on the other hand, is in a solute state at such treatment temperatures, restricting grain boundary mobility by the weaker solute drag effect.

Thermocalc calculations confirmed that, under equilibrium conditions, molybdenum is fully solute in austenite for all the investigated alloys (Figure 7). After transformation to ferrite, molybdenum can form a carbide of the type Mo_2C , having a hexagonally closed, packed crystal structure. In the lowest Mo-alloyed variant, the formation temperature was just above 600 °C and the expected carbide volume fraction was negligibly small. For higher Mo additions, however, the formation temperature increased, and the carbide volume fraction became substantially larger. The phase fraction of TiC is also shown. In the present alloys, the over-stoichiometric titanium content (equivalent to $\text{Ti}_{\text{tot}} \sim 3.4 \times \text{N}$ in mass percent), not being consumed as TiN, amounted to around 0.013%. At the low coiling temperature of 400 °C, Mo_2C precipitation was kinetically nearly impossible as the diffusivity of the molybdenum atom at that temperature was too limited for efficiently nucleating and growing carbide particles.

Thus, for low coiling temperature conditions, molybdenum was expected to be fully solute for all the alloys considered here. Applying a high coiling temperature (600 °C), on the contrary, allowed part of the molybdenum to be precipitated as Mo₂C particles, according to the ThermoCalc calculations (Figure 7). It is also possible that some fraction of molybdenum co-precipitates with Ti or Nb, yet this amount should be fairly small. Both types of particles have been recently observed experimentally in nearly the same steel under similar processing conditions [25].

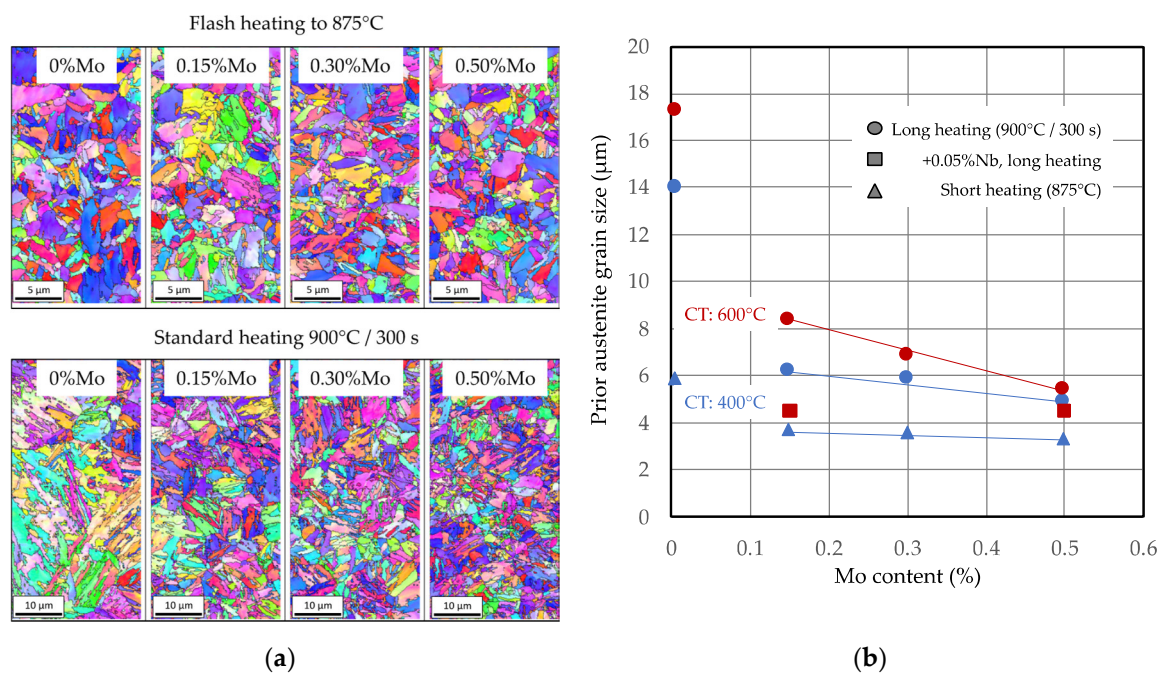


Figure 6. (a) Electron back scattering diffraction inverse pole figure micrographs of heat-treated steels (CT: 400°C) after quenching; (b) average prior austenite grain size of the various alloys and processing conditions.

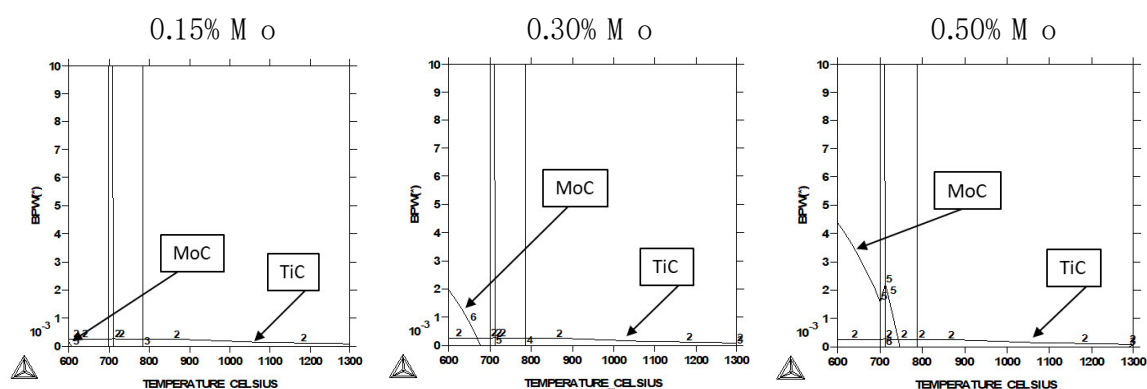


Figure 7. ThermoCalc calculations (database SSOL4) of stable carbide phases of molybdenum and titanium in the present steels.

3.3. Hydrogen Accumulation Measurements

Hydrogen desorption curves obtained from the samples treated by the short heating cycle are shown in Figure 8. The desorption peak characteristics of the samples produced with low coiling temperatures were not significantly influenced by the molybdenum alloy content. Their peak maxima were lower than those of the Mo-free base alloy, while the peak center positions were nearly the same. For samples produced with high coiling temperatures, however, the desorption peak maxima reached higher values and notably shifted towards higher temperatures with increasing molybdenum alloy

content. Accordingly, the accumulated hydrogen amount increased with the molybdenum content. All measured desorption peak maxima were located between 105 °C and 130 °C. Additionally, the 0.5% Mo alloyed steel exhibited a small desorption peak at approximately 315 °C after coiling at a high temperature, indicating the presence of stronger hydrogen traps in this steel. The amount of accumulated hydrogen in the samples (Figure 9) was derived from the desorption curves by numerical integration.

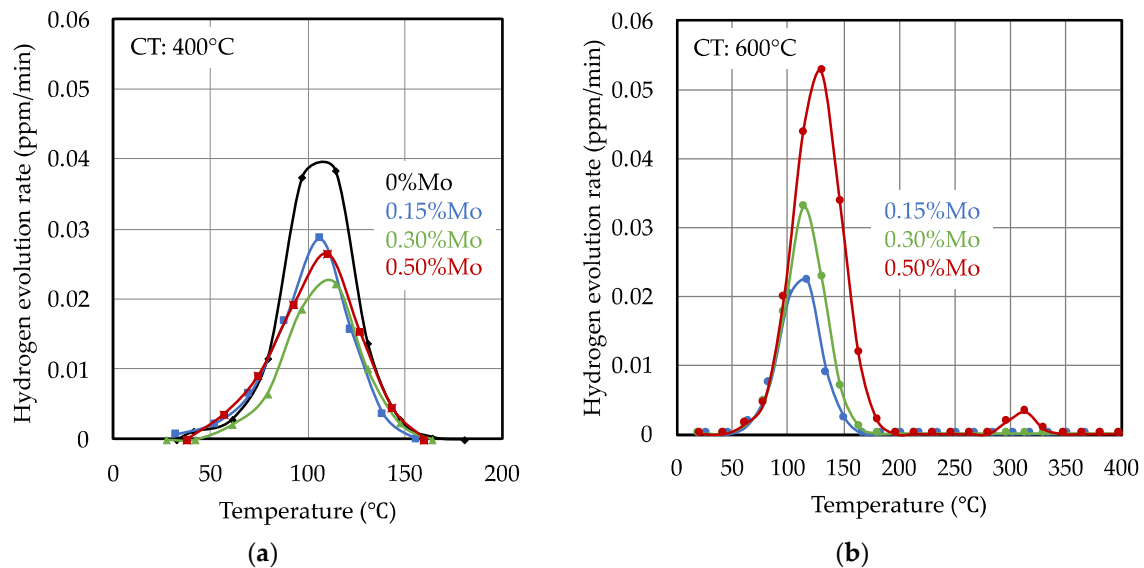


Figure 8. Thermal desorption spectra of bake hardened steels after 48 h of hydrogen charging in 10% ammonium thiocyanate solution. (a) Low coiling temperature (400 °C) and (b) high coiling temperature (600 °C).

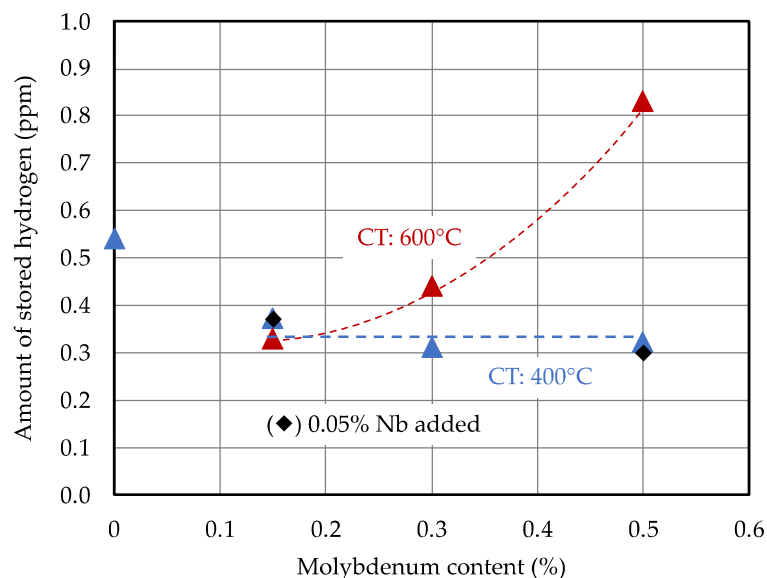


Figure 9. Thermal desorption spectra of quenched and bake hardened steels after 48 h of hydrogen charging in 10% ammonium thiocyanate solution.

For the low coiling temperature, the hydrogen content was nearly equal for the different molybdenum alloy content levels and clearly lower than in the Mo-free base alloy. The addition of niobium did not enhance the amount of accumulated hydrogen in comparison to the corresponding Mo-only alloy variant. Thus, no additional reversible hydrogen traps originated from niobium microalloying under the current processing conditions. Applying the coiling temperature of 600 °C to

the higher Mo-alloyed steels resulted in a significant increase in the accumulated hydrogen content. This observation, and the characteristics of the TDA curves, allows us to make the conclusion that a significant number of hydrogen traps with increased binding energy appeared. These traps were likely related to the incomplete dissolution of molybdenum carbide particles during the short heating cycle.

3.4. Delayed Cracking Performance

The base alloy showed a high sensitivity to hydrogen embrittlement (Figure 10). The time-to-fracture was less than 30 h, even for steels with a very small PAGS. Variation of the grain size by using different heating conditions indicated that, for coarser PAGS, the time-to-fracture further decreased, to values below 10 h. For comparison, the data of a 1500 MPa PHS base alloy (22MnB5) [5] that was also heat-treated to different grain sizes are included in Figure 10. The behavior of delayed cracking resistance as a function of the PAGS was qualitatively similar. However, the absolute time-to-fracture value for the softer PHS grade at the same PAGS was significantly higher. This difference clearly demonstrates that hydrogen embrittlement sensitivity severely increases with the strength (carbon) level of such martensitic steels.

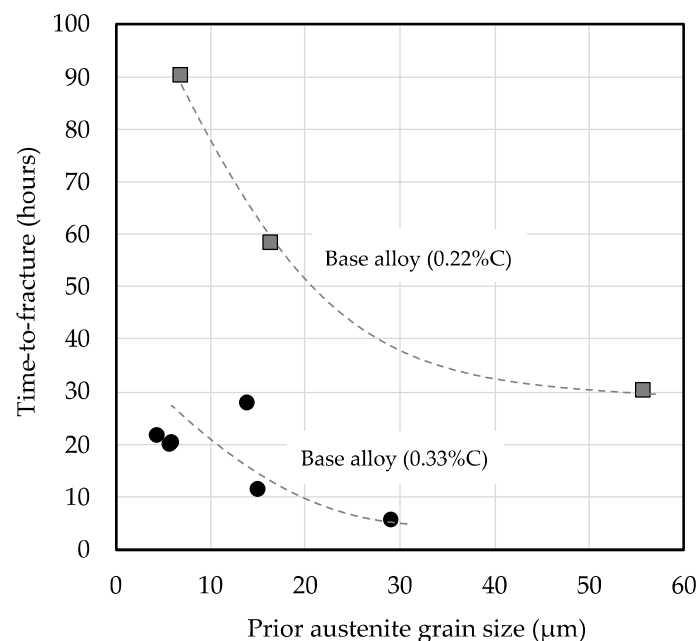


Figure 10. Influence of the PAGS in the base alloy on the delayed fracture resistance in 2000 (0.33%C) and 1500 MPa (0.22%C) press hardening steels after bake hardening treatment.

The measured average time-to-fracture data for the various processing conditions in the alloyed steels are displayed in Figure 11 as functions of the molybdenum alloy content. For the standard heat treatment condition, the values increased linearly with the molybdenum content, from around 30 h in the base alloy to more than 130 h when 0.5% Mo was added. The impact of coiling temperature on the delayed cracking resistance was marginal under the standard heat treatment condition. The addition of 0.05% Nb resulted in further extension of the time-to-fracture by 20–50 h. However, the beneficial effect of molybdenum addition on delayed cracking resistance was significantly weaker after the short heat treatment cycle. The improvement found for lower Mo additions (0.15%–0.30%) was comparable to that achieved by maximizing PAGS refinement (Figure 10). Only the highest degree of Mo addition resulted in a markedly better performance. There was still a significant difference in the delayed cracking resistance of the 0.5% Mo-alloyed steel depending on the coiling temperature (Figure 9). Using the higher coiling temperature in this alloy variant in combination with a short heating cycle resulted in the incomplete dissolution of the molybdenum carbide precipitates, reducing the level of

solute (segregated) molybdenum as well as increasing the amount of reversibly trapped hydrogen (Figure 8b).

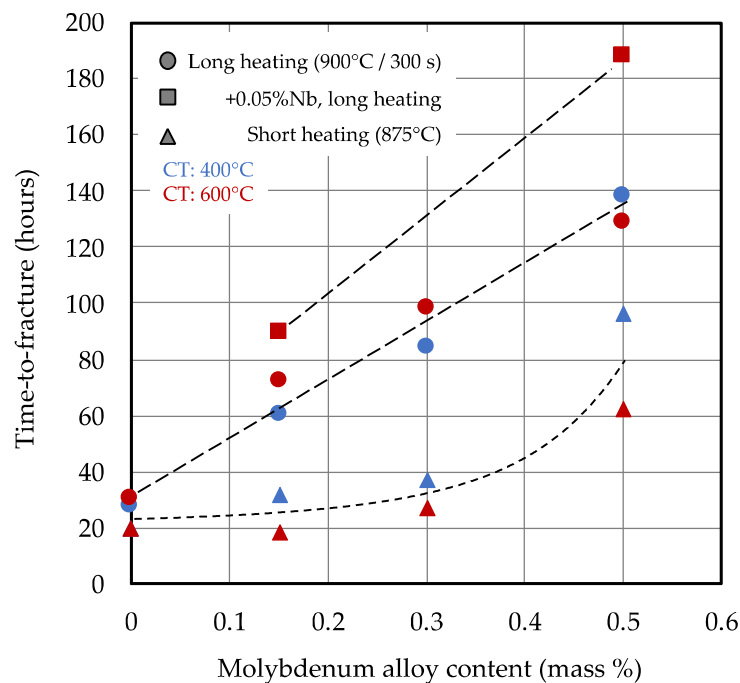


Figure 11. Delayed cracking resistance as function of the molybdenum alloy addition in 2000 MPa press hardening steel after bake hardening treatment.

In summary, it can be stated that the delayed cracking resistance linearly increased with the molybdenum alloy content for the standard heat treatment cycle, and niobium microalloying further improved the performance. When applying a short heat treatment cycle, only molybdenum additions above 0.3% brought significant performance improvement; however, critically, this depended on the coiling temperature.

3.5. Grain Boundary Segregation Analysis

The spatial distribution of the alloying elements, carbon, boron, molybdenum and manganese, along the direction that is normal for a prior austenite grain boundary was analyzed using three-dimensional (3D) atom probe tomography (APT). Respective elemental maps are shown in Figure 12a for the 0.5% Mo alloy coiled at lower temperatures and treated by the short cycle. Carbon, boron and molybdenum were strongly segregated along a line, representing a prior austenite grain boundary, whereas manganese exhibited a very weak segregation in this area. One-dimensional (1D) concentration profiles across the prior austenite grain boundary indicate that the concentration of molybdenum was approximately four times higher than in the grain bulk (Figure 12b). The segregation of carbon was even stronger, reaching a factor of approximately seven, while boron appeared to segregate nearly completely to the boundary. With regard to the later discussion, it is important to note here that the concentration enhancement was not strictly confined to the boundary itself, since the neighboring regular grain area also revealed significantly increased concentrations of the segregating elements. The present findings are in very good agreement with more detailed APT work done by Li et al. on similar quenchable Mn-B steels [26,27]. They pointed out that more carbon atoms exist in the same given boundary area of Mo-added steel than in that of Mo-free steel. In our study, while Mo and B segregated by the non-equilibrium mechanism only to the prior austenite grain boundary, carbon, in addition, segregated to boundaries formed in the martensite sub-structure based on an equilibrium mechanism. Due to the low martensite start temperature (<400 °C), the diffusion range of

molybdenum was far too low to allow equilibrium segregation to such boundaries, while boron was already completely depleted from the matrix before the martensite transformation.

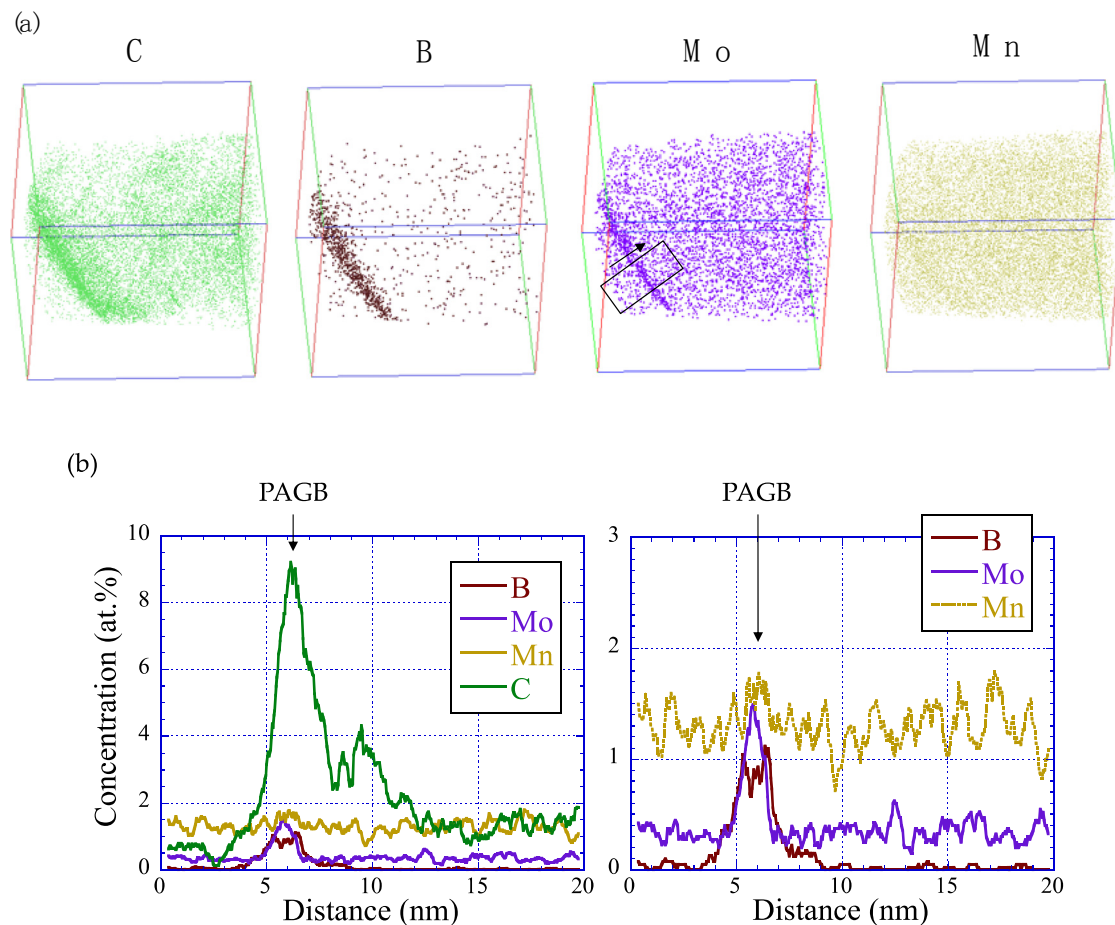


Figure 12. Atom probe tomography results of the region around the prior austenite grain boundary (PAGB) of the 0.5% Mo alloy (CT: 400 °C, short heat treatment cycle). (a) The 3D elemental maps of the elements, carbon, boron, molybdenum and manganese, in a reconstruction volume of 85 nm × 85 nm × 158 nm; (b) the 1D concentration profiles in the area and direction indicated in (a).

4. Discussion

The experimentally observed delayed cracking performance indicated that the physical status of the alloying elements, i.e., solute or precipitated, as well as the spatial distribution of solutes and particles within the microstructure, are important parameters. The possible interactions with respect to damage incubation and propagation will now be discussed.

4.1. Grain Boundary Related Effects

A network of mostly equiaxed polygonal austenite grains forms during the heat treatment of the cold-rolled elongated grain structure. An intergranular crack passing along the prior austenite grain boundaries in a martensitic steel is deflected by an average angle of 60 degrees when encountering a triple boundary junction. The energy required to propagate such an intergranular crack must increase with the encountered number of such deflections. Thus, refinement of the PAGS inherently enhances the resistance against intergranular cracking. Secondly, PAGS refinement increases the total grain boundary surface, consequently decreasing the specific concentration of impurity atoms per unit area and thus reducing the severity of the HEDE mechanism [3]. However, hydrogen occupation of the prior austenite grain boundary still saturates when high amounts of hydrogen have been accumulated

in the steel. Grain boundary segregation of solute molybdenum and niobium enhances the grain boundary cohesion, as mentioned before [16,17], thus counteracting the deleterious effect of hydrogen. The extent of grain boundary segregation for these alloying elements depends on the prior conditioning of the steel. In this respect, the standard heat treatment cycle (900 °C for 300 s) allows a more pronounced segregation than the short heat treatment cycle (875 °C peak). Higher coiling temperatures can lead to the more pronounced precipitation of alloy carbides, which reduces the amount of solute. Higher heat treatment temperatures and longer cycle durations allow for the re-dissolution of such alloy carbides, either in part (Nb) or completely (Mo).

Due to the high concentration of interstitial carbon in and near the PAGB, which is further enhanced by molybdenum alloying [26], it is feasible that less hydrogen can be accommodated by the grain boundary, since potential sites are already occupied by carbon atoms. This possibility was also suggested by Masutmoto et al. [28] based on density functional theory calculations. The effect can partially contribute to the observed improvement in delayed cracking resistance with increasing molybdenum content. Under conditions leading to a less pronounced PAGB segregation of molybdenum, as is the case for the short heat treatment cycle, this beneficial effect is expected to diminish.

The very high carbon concentration in the immediate neighborhood of the austenite grain boundary raises the question of whether this region can actually transform into martensite under the present processing conditions or whether it remains as retained austenite after quenching. Austenite provides a high solubility for hydrogen and can act as a potent trap. Unfortunately, with the analytical techniques used in this study, it was not possible to identify the presence of these hypothetically very thin austenite films. Thus, their possible influence on delayed cracking behavior is not considered here.

4.2. Interaction with Point Defects

Faulkner [29] pointed out that only solutes with high binding energies with vacancies (B, Mo, and Nb) are eligible for non-equilibrium segregation at PAGBs, whereas solutes such as Cr and Mn, which have low binding energies with vacancies are not segregated there. The binding energy between a vacancy and Mo has been reported as being 0.38 and 0.43 eV, while those between a vacancy and Nb have even higher values of 0.60 and 0.52 eV in ferrite and austenite, respectively [30].

Ab-initio calculations by Geng et al. [13] revealed that hydrogen forms complexes with vacancies, of which Vac-H₁ and Vac-H₂ both have a binding energy of around 0.63 eV and are thus energetically the most favorable ones. Thus, each vacancy preferably traps up to two hydrogen atoms. Furthermore, it was suggested that the clustering of Vac-H complexes occurs with linear arrangement in the <111> direction or as planar defects on the {110} or {100} planes. The formation of vacancy rows along <111>, representing the slip direction, can promote dislocation movement via the HELP mechanism. On the other hand, the planar clustering of vacancies on the {100} cleavage plane may initiate cracking with a brittle appearance. The type of locally acting damage mechanism depends also on the orientation of the crystallite with respect to the acting stress tensor.

Vacancy stabilization due to the formation of hydrogen–vacancy complexes above the amount determined by thermal equilibrium leads to vacancy super-saturation [31] being the basis of the HESIV mechanism. Additional vacancies are generated by the cutting or climbing of dislocations, which in turn is facilitated by the HELP mechanism. Vacancy super-saturation causes micro-void formation, typically in the immediate vicinity of the prior austenite and block boundaries (Figure 13). Micro-void coalescence leads to macroscopic fracturing, with a surface appearance of ductile failure.

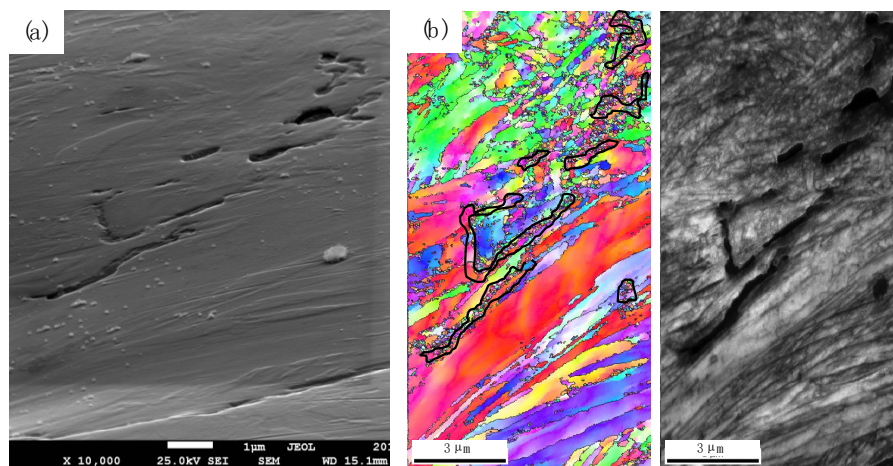


Figure 13. (a) Scanning electron micrograph of micro-void formation and coalescence due to the hydrogen-enhanced strain-induced vacancy mechanism (HESIV); (b) EBSD analysis of micro-void location at prior austenite and block boundaries within the martensitic microstructure.

Due to the binding energy of solute molybdenum or niobium with vacancies, it is feasible that the vacancy mobility is significantly lowered, since the diffusivity of the respective solute alloy atoms is extremely small at room temperature. Accordingly, the arrangement of hydrogen–vacancy clusters into planar or linear structures should be obstructed, thus impeding the incubation of hydrogen-induced damage. Furthermore, niobium and molybdenum have a pronounced attractive interaction with dislocations due to their large atom size ($Nb > Mo \gg Fe$), thus effectively reducing the mobility of dislocations (this effect also causes the well-known significant recrystallization delay of Mo- and Nb-alloyed steels upon annealing after cold deformation). The segregation of solute niobium atoms to dislocations, provoking a “niobium-induced Cottrell effect”, was directly shown by Takahashi et al. [32], using APT. In addition, mobile vacancies are required for enabling dislocation climbing. Thus, such solute-defect interactions that restrict dislocation mobility also counteract the HELP mechanism.

4.3. Solute Alloy Effects

It is reasonable to assume that the magnitude of the described effects is primarily related to the concentration of solute alloy atoms. This is manifested by a direct relationship in which time-to-fracture linearly increases with the molybdenum content (Figure 11) after applying the standard heat treatment. For the short heat treatment, this correlation is weaker and not linear, which may be due to the less pronounced segregation of molybdenum atoms to the PAGB region. Furthermore, some of the molybdenum carbide particles that were precipitated during coiling at the higher temperature might not have re-dissolved, thus resulting in a lower number of solute atoms. The importance of segregation relates to experimental observations that the region near the PAGB appears to be the most active one with regard to hydrogen-induced damage incubation [18,33]. Moving dislocations pile up against high-angle grain boundaries, thereby transporting hydrogen towards the PAGB and generating high local strain fields that attract diffusible hydrogen. High-angle grain boundaries also act as sinks for vacancies, so that hydrogen is also transported towards the boundary by the flux of hydrogen–vacancy complexes upon the application of mechanical stress [34].

Substitutional molybdenum atoms in the bcc iron lattice act as weak hydrogen trapping sites, according to Kim et al. [35]. Hagi [36] found that molybdenum alloying reduces hydrogen diffusivity in pure bcc iron, which was explained as being a consequence of local lattice distortion by the substitutional Mo atom, as well as its chemical interaction with hydrogen. Accordingly, the presence of molybdenum in the substitutional solution adds a large number of reversible hydrogen traps to the matrix of the present steels and particularly to the near-PAGB region. Rehrl et al. [37] reported hydrogen trapping enthalpy values for solute molybdenum and NbC precipitates of 5–13 kJ/mol and 16–23 kJ/mol, respectively. It

is feasible that a high spatial frequency of weak hydrogen traps with a very short mean-free distance leads to a more balanced hydrogen distribution in the steel, thus obstructing localized hydrogen accumulation to a critically high level.

4.4. Precipitate Interactions

In the present steels, carbide particles are formed, which are able to pin grain boundaries and dislocations and potentially act as hydrogen traps. The TEM micrographs in Figure 14 reveal the precipitation state of NbC and ferrous carbides (so-called ϵ -carbides) in a Nb microalloyed sample that was coiled at 600 °C. The ϵ -carbides, having a hexagonal close-packed structure, can establish several orientation relationships with the bcc iron host lattice, resulting in coherent or semi-coherent particle–matrix interfaces [38]. Using the different orientation relationships with the matrix, the ϵ -carbide and NbC could be separately displayed in dark-field images. Figure 14a shows the dark-field image of ϵ -carbides while Figure 14b shows that of NbC. This result implies that the fine ϵ -carbides that were predominantly precipitated during the bake hardening treatment covered most of the pre-existing NbC particles. Craig [39] considered ϵ -carbides acting as hydrogen-attractive trapping sites with an estimated trapping energy of 13 kJ/mol. Additionally, a high vacancy concentration was predicted in the particle-to-matrix interfacial area, since the silicon contained in these alloys diffuses away from the precipitate at a faster diffusion speed than the self-diffusion speed of iron.

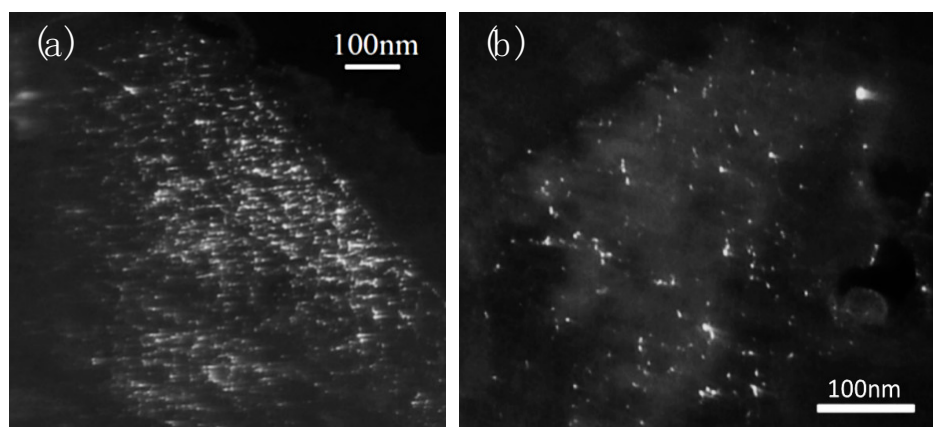


Figure 14. Thin foil transmission dark-field electron microscopy. (a) Orientation showing ϵ -carbide population appearing in all alloy variants after bake hardening treatment; (b) orientation showing NbC distribution in the 0.05% Nb microalloyed steel.

In the niobium microalloyed variants of the investigated steels, the niobium content precipitated nearly to completeness as NbC particles (Figure 14b) and partially as Ti,Nb(C,N). Less than 30 ppm Nb can exist in the solution at an austenitizing temperature of 900 °C in the standard heat treatment cycle, according to calculations using established solubility products [40]. Nucleation and growth conditions allowing the formation of microalloy precipitates are only given during the processing stages before final quenching. According to Wei et al. [41], incoherent particles do not act as hydrogen-attractive traps during hydrogen charging at room temperature. Thus, a significant contribution of microalloy carbides to hydrogen trapping was not expected under the current test conditions. Indeed, TDS analysis of the niobium microalloyed variants did not reveal a higher amount of stored hydrogen than in the Mo-only steels (Figure 9). However, the finely dispersed niobium carbides restricted the austenite grain growth during the austenitizing treatment by boundary pinning. The PAGS refining effect is obvious in the present steels, especially for those with a lower Mo content (Figure 6b). However, the grain size reduction appeared to only account for a comparatively small improvement in the time-to-fracture. Therefore, it is suggested that the major contribution of finely dispersed microalloy precipitates to the delayed cracking resistance is based on impeding dislocation mobility, i.e.,

obstructing the HELP mechanism [42]. A high particle density is important for maximizing this HELP obstructing effect, since a shorter mean-free particle distance provides stronger dislocation pinning. The amount of microalloy (Nb, Ti) that can be dissolved during the slab soaking treatment of a medium carbon steel, such as the present PHS, is limited. Hence, the particle density can only be increased by keeping the average particle size as small as possible. According to Seol et al. [43], molybdenum alloying enables a synergy with regard to microalloy precipitation. Thereby, molybdenum initially assists nucleation of the microalloy carbide and subsequently restricts its growth by forming a Mo-rich shell around a microalloy-rich core. This mechanism was found to enhance the population density of ultra-fine NbC particles [5,25]. The amount of molybdenum engaged in such particles is apparently smaller than the amount of microalloying elements. Thus, less than 0.07 mass percent of Mo should be withdrawn from the solute state by co-precipitation in the case of the present alloys.

5. Conclusions

This investigation has shown that the standard alloy 32MnB5 that is used for 2000 MPa press hardening steel is severely sensitive to hydrogen-induced delayed cracking. Alloy modification by adding molybdenum and niobium substantially improved the delayed cracking resistance to a level that is acceptable for automotive applications. These results refer to the bake hardened condition of the martensitic steel and thus represent the performance of the respective components during the vehicle-use phase.

The achieved optimization mainly originates from the refinement of the prior austenite grain structure and interaction of solute molybdenum, as well as the niobium-based precipitates with microstructural defects such as dislocations and vacancies. In this way, hydrogen-induced damage incubation by the HEDE, HELP and HESIV mechanisms is obstructed. The current results, however, do not indicate that hydrogen trapping by these alloying elements or their respective alloy carbide precipitates plays the decisive role in reducing delayed cracking sensitivity under the investigated circumstances.

Molybdenum is most effective in reducing hydrogen embrittlement when the element is in a substitutional solution and is pronouncedly segregated to the prior austenite grain boundary. Niobium deploys its beneficial effects in the form of niobium carbide precipitates, which should be of ultra-fine size and homogeneously distributed. Synergies between the two alloying elements became evident, reflecting the highest resistance against hydrogen-induced for Mo-Nb co-alloyed press hardening steels. This study also provides guidelines with regard to the most suitable processing conditions for maximizing these alloys' effects.

Author Contributions: Conceptualization, H.M. and T.S.; methodology, T.S.; experimental investigation, T.S.; writing—original draft preparation, H.M.; review and final editing, H.M.; T.S. All authors have read and agreed to the published version of the manuscript.

Funding: This research was funded by the International Molybdenum Association (IMOA), London, UK.

Acknowledgments: The authors wish to sincerely thank J. Takahashi, Nippon Steel, for providing the analytical results of atom probe tomography data.

Conflicts of Interest: The authors declare no conflict of interest.

References

1. Hikida, K.; Nishibata, T.; Kikuchi, H.; Suzuki, T.; Nakayama, N. Development of TS1800fVIPa Grade Hot Stamping Steel Sheet. *Mater. Jpn.* **2013**, *52*, 68–70. [[CrossRef](#)]
2. Wang, J.; Enloe, C.; Singh, J.; Horvath, C. Effect of Prior Austenite Grain Size on Impact Toughness of Press Hardened Steel. *SAE Int. J. Mater. Manuf.* **2016**, *9*, 488–493. [[CrossRef](#)]
3. Mohrbacher, H. Property Optimization in As-Quenched Martensitic Steel by Molybdenum and Niobium Alloying. *Metals* **2018**, *8*, 234. [[CrossRef](#)]

4. Cobo, S.; Sturel, T.; Aouafi, A.; Allely, C.; Cornette, D. Hydrogen Embrittlement Resistance of Al-Si coated 1.8GPa Press Hardened Steel Solutions for Body- in-White (BIW) Applications. In Proceedings of the 7th International Conference on Hot Sheet Metal Forming of High Performance Steel, Lulea, Sweden, 2–5 June 2019; Oldenburg, M., Hardell, J., Casellas, D., Eds.; pp. 179–189.
5. Uranga, P.; Shang, C.-J.; Senuma, T.; Yang, J.-R.; Guo, A.-M.; Mohrbacher, H. Molybdenum alloying in high-performance flat-rolled steel grades. *Adv. Manuf.* **2020**, *8*, 15–34. [[CrossRef](#)]
6. Nagumo, M. Advances in Physical Metallurgy and Processing of Steels. Function of Hydrogen in Embrittlement of High-strength Steels. *ISIJ Int.* **2001**, *41*, 590–598. [[CrossRef](#)]
7. Valentini, R.; Tedesco, M.M.; Corsinovi, S.; Bacchi, L.; Villa, M. Investigation of Mechanical Tests for Hydrogen Embrittlement in Automotive PHS Steels. *Metals* **2019**, *9*, 934. [[CrossRef](#)]
8. Irani, J.J. Fracture of Martensite with particular reference to ausformed martensite. In *Physical Properties of Martensite and Bainite*; Special Report 93; The Iron and Steel Institute: London, UK, 1965; pp. 193–203.
9. Mohrbacher, H.; Morris, J.W.; Krauss, G. Fundamentals and Practical Approaches of Optimizing Martensitic Steels for Use under Severe Operating Conditions. In Proceedings of the International Symposium on Wear Resistant Alloys for the Mining and Processing Industry, Campinas, São Paulo, Brazil, 4–7 May 2015; Mohrbacher, H., Ed.; TMS: Warrendale, PA, USA, 2018; pp. 93–158.
10. Nakasato, F.; Tsumura, T.; Ueda, T.; Murai, N. *Development of Delayed Fracture Resistant High-Strength Steel ADS-2*; The Sumitomo Search No.37; Sumitomo Metals Corporation: Tokyo, Japan, 1988; pp. 1–12.
11. Jiang, D.-E.; Carter, E.A. First principles assessment of ideal fracture energies of materials with mobile impurities: Implications for hydrogen embrittlement of metals. *Acta Mater.* **2004**, *52*, 4801–4807. [[CrossRef](#)]
12. Yuasa, M.; Amemiya, T.; Mabuchi, M. Enhanced grain boundary embrittlement of an Fe grain boundary segregated by hydrogen (H). *J. Mater. Res.* **2012**, *27*, 1589–1597. [[CrossRef](#)]
13. Geng, W.-T.; Freeman, A.J.; Olson, G.B.; Tateyama, Y.; Ohno, T. Hydrogen-Promoted Grain Boundary Embrittlement and Vacancy Activity in Metals: Insights from Ab Initio Total Energy Calculations. *Mater. Trans.* **2005**, *46*, 756–760. [[CrossRef](#)]
14. Takasawa, K.; Wada, Y.; Ishigaki, R.; Kayano, R. Effects of Grain Size on Hydrogen Environment Embrittlement of High Strength Low Alloy Steel in 45 MPa Gaseous Hydrogen. *Mater. Trans.* **2010**, *51*, 347–353. [[CrossRef](#)]
15. Komazaki, S.-I.; Watanabe, S.; Misawa, T. Influence of Phosphorus and Boron on Hydrogen Embrittlement Susceptibility of High Strength Low Alloy Steel. *ISIJ Int.* **2003**, *43*, 1851–1857. [[CrossRef](#)]
16. Geng, W.-T.; Freeman, A.J.; Olson, G.B. Influence of alloying additions on grain boundary cohesion of transition metals: First-principles determination and its phenomenological extension. *Phys. Rev. B* **2001**, *63*, 165415. [[CrossRef](#)]
17. Lejcek, P. *Grain Boundary Segregation in Metals*; Springer Series in Materials Science; Springer: Berlin/Heidelberg, Germany, 2010; pp. 173–183.
18. Nagao, A.; Smith, C.D.; Dadfarnia, M.; Sofronis, P.; Robertson, I.M. The role of hydrogen in hydrogen embrittlement fracture of lath martensitic steel. *Acta Mater.* **2012**, *60*, 5182–5189. [[CrossRef](#)]
19. Birnbaum, H.; Sofronis, P. Hydrogen-enhanced localized plasticity—A mechanism for hydrogen-related fracture. *Mater. Sci. Eng. A* **1994**, *176*, 191–202. [[CrossRef](#)]
20. Nagumo, M. Hydrogen related failure of steels—A new aspect. *Mater. Sci. Technol.* **2004**, *20*, 940–950. [[CrossRef](#)]
21. Tateyama, Y.; Ohno, T. Atomic-scale Effects of Hydrogen in Iron toward Hydrogen Embrittlement: Ab-initio Study. *ISIJ Int.* **2003**, *43*, 573–578. [[CrossRef](#)]
22. Miyamoto, G.; Iwata, N.; Takayama, N.; Furuhashi, T. Mapping the parent austenite orientation reconstructed from the orientation of martensite by EBSD and its application to ausformed martensite. *Acta Mater.* **2010**, *58*, 6393–6403. [[CrossRef](#)]
23. Mohrbacher, H.; Tolotti de Almeida, D.; Correa de Souza, J.H. Material Development and Qualification of Manufacturing Technology for Hot Stamping of Heavy Gage Components. In Proceedings of the 7th International Conference on Hot Sheet Metal Forming of High Performance Steel, Lulea, Sweden, 2–5 June 2019; Oldenburg, M., Hardell, J., Casellas, D., Eds.; pp. 301–309.
24. Ishikawa, K.; Nakamura, H.; Homma, R.; Fujioka, M.; Hoshino, M. Effect of Molybdenum Content on the Combined Effect of Boron and Molybdenum on Hardenability of Low-Carbon Boron-Added Steels. *ISIJ Int.* **2018**, *58*, 551–560. [[CrossRef](#)]

25. Jo, M.C.; Yoo, J.; Kim, S.; Kim, S.; Oh, J.; Bian, J.; Sohn, S.S.; Lee, S. Effects of Nb and Mo alloying on resistance to hydrogen embrittlement in 1.9 GPa-grade hot-stamping steels. *Mater. Sci. Eng. A* **2020**, *789*, 139656. [[CrossRef](#)]
26. Li, Y.; Ponge, D.; Choi, P.-P.; Raabe, D. Segregation of boron at prior austenite grain boundaries in a quenched martensitic steel studied by atom probe tomography. *Scr. Mater.* **2015**, *96*, 13–16. [[CrossRef](#)]
27. Li, Y.; Ponge, D.; Choi, P.-P.; Raabe, D. Atomic scale investigation of non-equilibrium segregation of boron in a quenched Mo-free martensitic steel. *Ultramicroscopy* **2015**, *159*, 240–247. [[CrossRef](#)]
28. Matsumoto, R.; Riku, M.; Taketomi, S.; Miyazaki, N. Hydrogen–Grain Boundary Interaction in Fe, Fe–C, and Fe–N Systems. *Prog. Nucl. Sci. Technol.* **2011**, *2*, 9–15. [[CrossRef](#)]
29. Faulkner, R. Combined grain boundary equilibrium and non-equilibrium segregation in ferritic/martensitic steels. *Acta Met.* **1987**, *35*, 2905–2914. [[CrossRef](#)]
30. Faulkner, R.G.; Song, S.-H.; Flewitt, P.E.J. Determination of impurity-point defect binding energies in alloys. *Mater. Sci. Technol.* **1996**, *12*, 904–910. [[CrossRef](#)]
31. Iwamoto, M.; Fukai, Y. Superabundant Vacancy Formation in Iron under High Hydrogen Pressures: Thermal Desorption Spectroscopy. *Mater. Trans. JIM* **1999**, *40*, 606–611. [[CrossRef](#)]
32. Takahashi, J.; Kawakami, K.; Hamada, J.-I.; Kimura, K. Direct observation of niobium segregation to dislocations in steel. *Acta Mater.* **2016**, *107*, 415–422. [[CrossRef](#)]
33. Nagao, A.; Smith, C.D.; Dadfarnia, M.; Sofronis, P.; Robertson, I.M. Interpretation of Hydrogen-induced Fracture Surface Morphologies for Lath Martensitic Steel. *Procedia Mater. Sci.* **2014**, *3*, 1700–1705. [[CrossRef](#)]
34. Momotani, Y.; Shibata, A.; Terada, D.; Tsuji, N. Effect of strain rate on hydrogen embrittlement in low-carbon martensitic steel. *Int. J. Hydrog. Energy* **2017**, *42*, 3371–3379. [[CrossRef](#)]
35. Kim, K.T.; Park, J.K.; Lee, J.Y.; Hwang, S.H. Effect of alloying elements on hydrogen diffusivity in α -iron. *J. Mater. Sci.* **1981**, *16*, 2590–2596. [[CrossRef](#)]
36. Hagi, H. Effect of Substitutional Alloying Elements (Al, Si, V, Cr, Mn, Co, Ni, Mo) on Diffusion Coefficient of Hydrogen in α -Iron. *Mater. Trans. JIM* **1992**, *33*, 472–479. [[CrossRef](#)]
37. Rehrl, J.; Mraczek, K.; Pichler, A.; Werner, E. The Impact of Nb, Ti, Zr, B, V, and Mo on the Hydrogen Diffusion in Four Different AHSS/UHSS Microstructures. *Steel Res. Int.* **2013**, *85*, 336–346. [[CrossRef](#)]
38. Jack, K.H. Structural Transformations in the Tempering of High-Carbon Martensitic Steels. *J. Iron Steel Inst.* **1951**, *169*, 26–36.
39. Craig, B.D. On the elastic interaction of hydrogen with precipitates in lath martensite. *Acta Met.* **1977**, *25*, 1027–1030. [[CrossRef](#)]
40. Sharma, R.C.; Lakshmanan, V.K.; Kirkaldy, J.S. Solubility of niobium carbide and niobium carbonitride in alloyed austenite and ferrite. *Met. Mater. Trans. A* **1984**, *15*, 545–553. [[CrossRef](#)]
41. Wei, F.G.; Tsuzaki, K. Quantitative analysis on hydrogen trapping of TiC particles in steel. *Met. Mater. Trans. A* **2006**, *37*, 331–353. [[CrossRef](#)]
42. Zhang, S.; Wan, J.; Zhao, Q.; Liu, J.; Huang, F.; Huang, Y.; Li, X. Dual role of nanosized NbC precipitates in hydrogen embrittlement susceptibility of lath martensitic steel. *Corros. Sci.* **2020**, *164*, 108345. [[CrossRef](#)]
43. Seol, J.-B.; Na, S.-H.; Gault, B.; Kim, J.-E.; Han, J.-C.; Park, C.-G.; Raabe, D. Core-shell nanoparticle arrays double the strength of steel. *Sci. Rep.* **2017**, *7*, 42547. [[CrossRef](#)]

